Symmetry-protected mode coupling near normal incidence for narrow-band transmission filtering in a dielectric grating

J. M. Foley,[1,2,*] S. M. Young,[1,3] and J. D. Phillips[1,2]

[1]*Applied Physics Program, University of Michigan, Ann Arbor, Michigan 48109, USA*

[2]*Electrical Engineering and Computer Science Department, University of Michigan, Ann Arbor, Michigan 48109, USA*

[3]*Physics Department, University of Michigan, Ann Arbor, Michigan 48109, USA*

(Received 1 January 2014; revised manuscript received 20 March 2014; published 9 April 2014)

A narrow-band transmission filter is demonstrated near normal incidence that operates through relaxation of supported-mode selection rules and is explained in the context of group theory. We calculated the transverse magnetic and transverse electric dispersion relations of a dielectric grating in the subwavelength and near-wavelength region using finite element modal analysis and determine the modes' corresponding irreducible representations. Coupling to select transverse magnetic modes at normal incidence is optimized to yield broadband high reflectance that acts as the background for the transmission filter. While some modes couple at normal incidence, others are shown to remain inaccessible due to symmetry mismatch. Away from normal incidence, the reduced symmetry relaxes the selection rules, enabling weak coupling between the incident field and these symmetry-protected modes. This weak coupling produces narrow transmission bands within the opaque background. Furthermore, by choosing the plane of incidence to include or exclude the grating periodicity, we show that orthogonal mode sets can independently be selected to couple to the incident light, yielding separate transmission bands. This spectral filtering is experimentally demonstrated with a suspended silicon grating in the infrared spectrum (7–14 μm), which agrees well with simulated transmittance spectra and modal analysis.

DOI: 10.1103/PhysRevB.89.165111 PACS number(s): 42.79.Dj, 42.79.Ci, 78.67.Pt, 42.70.Qs

I. INTRODUCTION AND SYSTEM

Over the past two decades, photonic crystals have enabled studies of many interesting physical phenomena and have been increasingly used in applications [1]. These periodic structures possess band structures that can be exploited to engineer the electromagnetic response of a given system, and are analogous to the electronic bands of crystalline materials [2,3]. Photonic crystal slabs, a specific class of photonic crystals, have their periodicity confined to a thin layer that is surrounded by a low-index material; consequently they have bands that extend into the light cone [4]. These leaky modes can be excited by incident plane waves to produce Fano line shapes [5–8] and similarly decay into the continuum when the excitation source is removed. The lifetime of an excited mode and its associated coupling strength to the continuum is largely determined by the mutual symmetry of the mode and permissible outgoing waves [4]. Select modes possess infinite lifetimes at zone center as a result of their symmetry mismatch with allowed radiation modes [9,10]. These symmetry-protected modes have recently been used to demonstrate high-quality factor resonances near normal incidence that may be exploited for various applications [11–13].

Particular one-dimensional photonic crystal slabs, often called high-contrast gratings, have demonstrated spectral engineering capabilities including ultrabroadband reflectors [14,15], two-dimensional lenses [16,17], and filters [8,12,18–23]. The presence of symmetry-protected modes exhibited by high-contrast gratings provide even further spectral engineering capabilities. For example, we recently reported a narrow-band transmission filter based on an optimized broadband reflector and symmetry-protected mode coupling in a single-layer dielectric grating [12]. In this paper we generalize and demonstrate symmetry-based selection rules for coupling to a set of transverse magnetic (TM) and a set of transverse electric (TE) modes using a group theoretical analysis and finite element simulations. Experimental validation is performed with a suspended silicon grating that operates in the infrared spectrum (7–14 μm).

Figure 1 shows a schematic of the investigated dielectric grating and its associated Brillouin zone. The grating is defined by its relative permittivity (ϵ_g), period (Λ), thickness (t), and fill factor (FF, defined as the ratio of the grating width to the grating period, w/Λ), as well as the surrounding material's relative permittivity (ϵ_s). The materials are assumed to be nonmagnetic, $\mu_g = \mu_s = 1$. We consider plane waves with the electric field perpendicular to the z axis ($\boldsymbol{E}_{xy}$, green dotted plane) and the magnetic field perpendicular to the x axis ($\boldsymbol{H}_{yz}$, red dashed plane) with a plane wave's incidence defined by its angle with respect to the normal in the xy plane (θ) and yz plane (φ). The grating's periodicity in the x direction limits the extent of the first Brillouin zone in the k_x direction while k_y and k_z remain unbounded. [Note that, strictly speaking, k_y is not a good quantum number, as the system lacks translation symmetry in the y direction. We refer here to the far-field (plane-wave) wave vector of incident or radiated fields associated with the resonant modes, defined by $k_y^2 = \omega_{k_x,k_z}^2/c^2 - k_x^2 - k_z^2$.]

Analyzing the symmetry of the grating's supported modes and incident plane waves can help us leverage selective mode coupling to produce narrow-band transmission filters using these structures. We will discuss mode coupling at normal incidence, Point I ($|k_y| > 0$, $\theta = \varphi = 0°$), and off-normal incidence in the xy and yz planes, Point II ($|k_y|,|k_x| > 0$, $\theta > 0°$), and Point III ($|k_y|,|k_z| > 0$, $\varphi = 0°$), respectively.

*foleyjm@umich.edu

 ©2014 American Physical Society

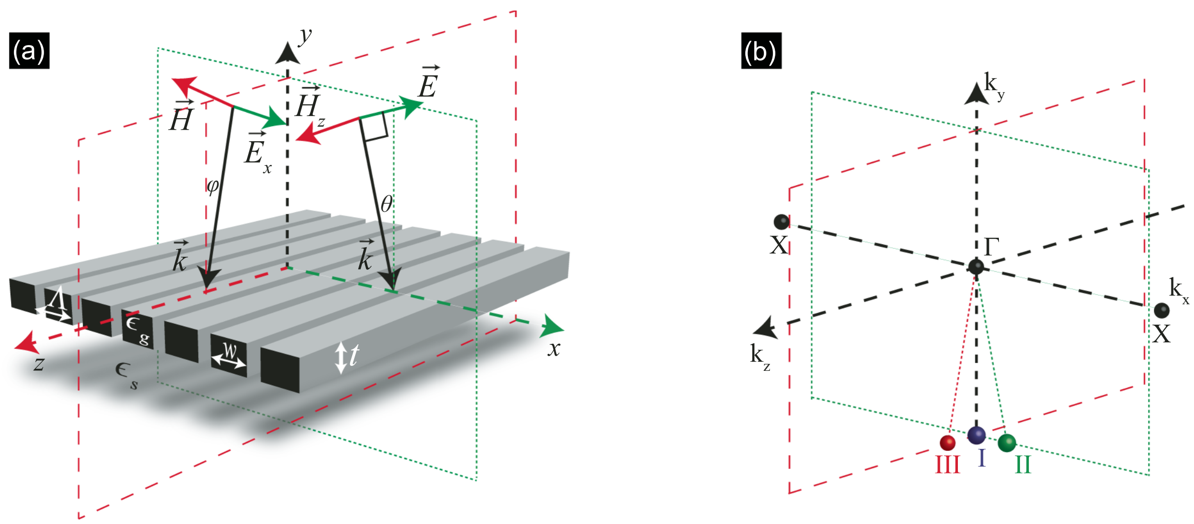

FIG. 1. (Color online) Grating schematic and its corresponding Brillouin zone with incident fields, dimensions, and material properties defined. (a) The grating includes its period (Λ), height (t), width (w, defined as $\Lambda \times FF$ where FF is the fill factor), and material permittivities for the grating (ϵ_g) and surrounding material (ϵ_s). The electric field lies parallel to the xy plane and the magnetic field lies parallel to the yz plane. The angles with respect to normal are θ and φ, which lie in the xy and yz planes, respectively. (b) The grating's Brillouin zone with analyzed incident wave vectors: Point I: normal incidence or $\theta = \varphi = 0^\circ$ ($k_x = k_z = 0, |k_y| > 0$), Point II: $\theta > 0^\circ$ ($|k_x|, |k_y| > 0, k_z = 0$), and Point III: $\varphi > 0^\circ$ ($k_x = 0$, and $|k_y|, |k_z| > 0$).

II. GROUP THEORETICAL ANALYSIS

The grating belongs to the D_{2h} point group, requiring the grating's supported modes at the Γ point ($\boldsymbol{k} = 0$) to have the same symmetry as the point group's irreducible representations [4]. Table I shows the character table of the D_{2h} point group, along with some guided modes of the grating, discussed in more detail later, that belong to each irreducible representation. To facilitate a group theoretical analysis, we calculated the dispersion relations for the grating using finite element methods. The modal analysis calculates the complex propagation constant using the weak formulation of Helmholtz equation expressed as a quadratic eigenvalue problem [24,25]. The resulting dispersion relations for TM polarized modes and the associated field profiles for several resonances are shown in Fig. 2 for a grating with: $\frac{t}{\Lambda} = 0.6$, $FF = 0.72$, $\epsilon_g = 11.7$, and $\epsilon_s = 1$. The dispersion relations show the guided modes, with solid bands representing modes that were calculated using the modal analysis. The dashed bands, in contrast, were estimated from scattering analysis due to their imaginary propagation constants being larger than the Brillouin zone, which makes them difficult to accurately calculate. Because of the grating periodicity in one direction, the dispersion relations are represented in a reduced zone scheme with the index contrast between the grating and surrounding material lifting the degeneracies at the zone boundaries ($k_x = \frac{\pi}{2}$) and zone center ($\boldsymbol{k} = 0$). The modes at zone center ($\boldsymbol{k} = 0$) are labeled with their irreducible representations, determined by using a reduction procedure [4] and by applying the symmetry operations of the D_{2h} point group to the simulated mode field profiles. These modes, with the exception of the zero-frequency mode, lie within the light cone as a consequence of the photonic crystal's slab design. Hence, phase matching is possible between these modes and incident light. The lowest-order leaky mode, TM_1^-, belongs to the B_{2u} irreducible representation. This mode is antisymmetric upon rotation about the z axis (C_{2z}) and reflection across the xz plane (σ_y), and symmetric upon reflection across the yz plane (σ_x), remembering the magnetic field is a pseudovector.

TABLE I. D_{2h} character table corresponding to the Γ point of the grating's reciprocal lattice with the analyzed grating modes associated with each irreducible representation.

D_{2h}	E	C_{2z}	C_{2y}	C_{2x}	i	σ_z	σ_y	σ_x	TM Modes	TE Modes
A_g	1	1	1	1	1	1	1	1	TM_2^-	
B_{1g}	1	1	−1	−1	1	1	−1	−1	TM_1^+, TM_3^-	
B_{2g}	1	−1	1	−1	1	−1	1	−1		TE_1^-, TE_3^-, TE_4^-
B_{3g}	1	−1	−1	1	1	−1	−1	1		TE_2^+
A_u	1	1	1	1	−1	−1	−1	−1		TE_2^-
B_{1u}	1	1	−1	−1	−1	−1	1	1		TE_1^+
B_{2u}	1	−1	1	−1	−1	1	−1	1	TM_1^-	
B_{3u}	1	−1	−1	1	−1	1	1	−1	TM_2^+	

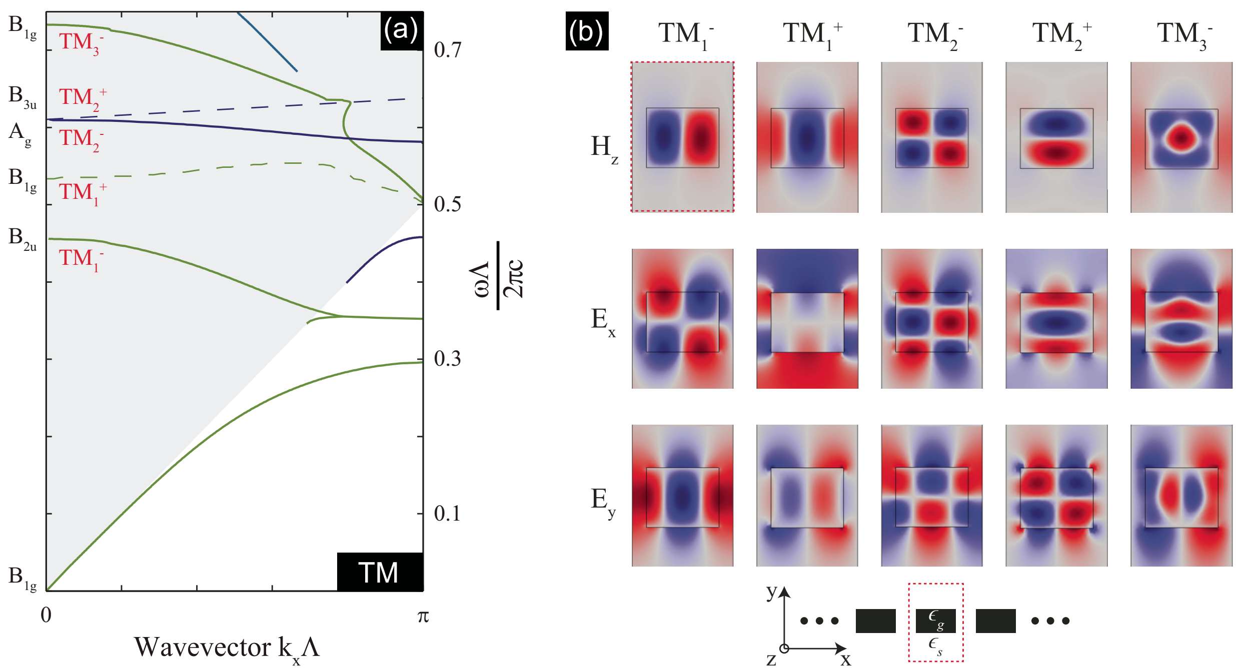

FIG. 2. (Color online) TM dispersion relations and field profiles for a grating with $\frac{t}{\Lambda} = 0.6$, $FF = 0.72$, $\epsilon_g = 11.7$, and $\epsilon_s = 1$. (a) The dispersion relations include even (blue) and odd (green) bands with respect to reflection across $y = 0$. Solid bands were calculated using a finite element modal analysis and dashed bands are estimated from scattering analysis. The modes at $k_x = 0$ are labeled with their Γ point (D_{2h} symmetry) irreducible representations and band definitions. The light cone is shown in light gray. (b) TM mode field profiles at $k_x = 0$ with a black line indicating the boundary between high and low permittivity regions. Below: grating simulation element, and directions defined.

We will show that at normal incidence a TM polarized plane wave cannot excite modes of this symmetry.

A normally incident TM polarized plane wave, $|k_y| > 0$, shown as Point I in Fig. 1(b), belongs to the reduced symmetry of the C_{2v}^y point group, where the superscript y indicates the symmetric rotation axis. The symmetry operations of this group (E, C_{2y}, σ_z, and σ_x) are summarized with its irreducible representations in Table II(a), along with the grating modes belonging to each representation. A wave with this polarization can couple to TM (but not TE) guided modes in the grating. For this coupling to occur, the phase matching condition must be met and the overlap integral between the incident field and the supported mode must be nonzero; this requires the mode and incident wave to belong to the same irreducible representation. The compatibility relations between Point I and the Γ point, determined by comparing the character tables for the relevant symmetry operations, give their mutual irreducible representations. These relations, summarized in Table II(b), show that each mode at Point I (C_{2v} point group) maps onto two modes at the Γ point (D_{2h} point group). The incident TM plane wave of Point I belongs to the B_1 irreducible representation, which matches the symmetry of the B_{1g} and B_{3u} Γ-point irreducible representations at Point I. This plane wave, thus, can couple to modes that belong to these two irreducible representations at the Γ point while the other modes are inaccessible or symmetry protected, see Table II(a); explicitly, modes TM_1^+, TM_2^+, and TM_3^- of Fig. 2 are all accessible at normal incidence, while modes TM_1^- and TM_2^- are symmetry protected. This symmetry matching is illustrated by the x component of the electric field

TABLE II. (a) C_{2v}^y character table and the analyzed grating modes associated with each irreducible representation, and (b) the compatibility relations between Point I and the Γ point.

C_{2v}	E	C_{2y}	σ_z	σ_x	TM Modes	TE Modes	Point I	Γ
A_1	1	1	1	1	TM_1^-, TM_2^-		A_1	A_g, B_{2u}
A_2	1	1	−1	−1		TE_1^-, TE_2^- TE_3^-, TE_4^-	A_2	B_{2g}, A_u
B_1	1	−1	1	−1	TM_1^+, TM_2^+ TM_3^-		B_1	B_{1g}, B_{3u}
B_2	1	−1	−1	1		TE_1^+, TE_2^+	B_2	B_{3g}, B_{1u}
(a)							(b)	

TABLE III. (a) C_s^{xy} character table and the analyzed grating modes associated with each irreducible representation, and (b) the compatibility relations between Point II and the Γ point.

C_s^{xy}	E	σ_z	TM Modes	TE Modes	Point II	Γ
A'	1	1	$\mathrm{TM}_1^-,\mathrm{TM}_1^+$ $\mathrm{TM}_2^-,\mathrm{TM}_2^+,\mathrm{TM}_3^-$		A'	$A_g, B_{1g}, B_{2u}, B_{3u}$
A''	1	−1		$\mathrm{TE}_1^-,\mathrm{TE}_1^+,\mathrm{TE}_2^-$ $\mathrm{TE}_2^+,\mathrm{TE}_3^-,\mathrm{TE}_4^-$	A''	$A_u, B_{2g}, B_{3g}, B_{1u}$
			(a)		(b)	

intensity shown in Fig. 2(b) where modes TM_1^+, TM_2^+, and TM_3^- share plane-wave symmetry in the x direction while modes TM_1^- and TM_2^- are antisymmetric in comparison.

To access the symmetry-protected modes, the incident wave vector can be moved off the k_y axis to Point II, which is maintained in the k_xk_y plane. Point II has the further reduced symmetry of the C_s^{xy} point group, with symmetry only upon reflection across the xy plane, σ_z. The C_s^{xy} character table and the modes associated with each irreducible representation, as well as the compatibility relations between Point II (C_s^{xy} point group) and the Γ point (D_{2h} point group) are given in Tables III(a) and III(b). This reduced symmetry relaxes the selection rules, illustrated by the mapping of four Γ-point irreducible representations onto each irreducible representation at Point II, as shown in Table III(a). An incident TM plane wave belongs to the A' irreducible representation. All the TM modes considered at Point II share this irreducible representation, as shown in Table III(a). Consequently, the modes that are symmetry protected at normal incidence can now couple to this off-normal incidence plane wave.

If instead we consider a plane wave with wave vector at Point III of Fig. 1, we maintain symmetry across the yz plane, σ_x, and introduce a y component of the magnetic field (H_y) to the plane wave. In addition to exciting TM modes, this wave can also couple to TE guided modes, provided they have the appropriate symmetry. Accordingly, the grating's TE dispersion relations were calculated using the modal analysis and are shown in Fig. 3 with field profiles of select modes illustrated. The C_s^{yz} character table with modes associated with each irreducible representation and the compatibility relations between Point III (C_s^{yz} point group) and the Γ point (D_{2h} point group) are shown in Tables IV(a) and IV(a). At Point III the incident plane wave belongs to the A'' irreducible representation of the C_s^{yz} point group, which shares the symmetry of several guided modes at Point III, as shown in Table IV(a). Thus, coupling to TE_1^-, TE_2^-, TE_3^-, and TE_4^-

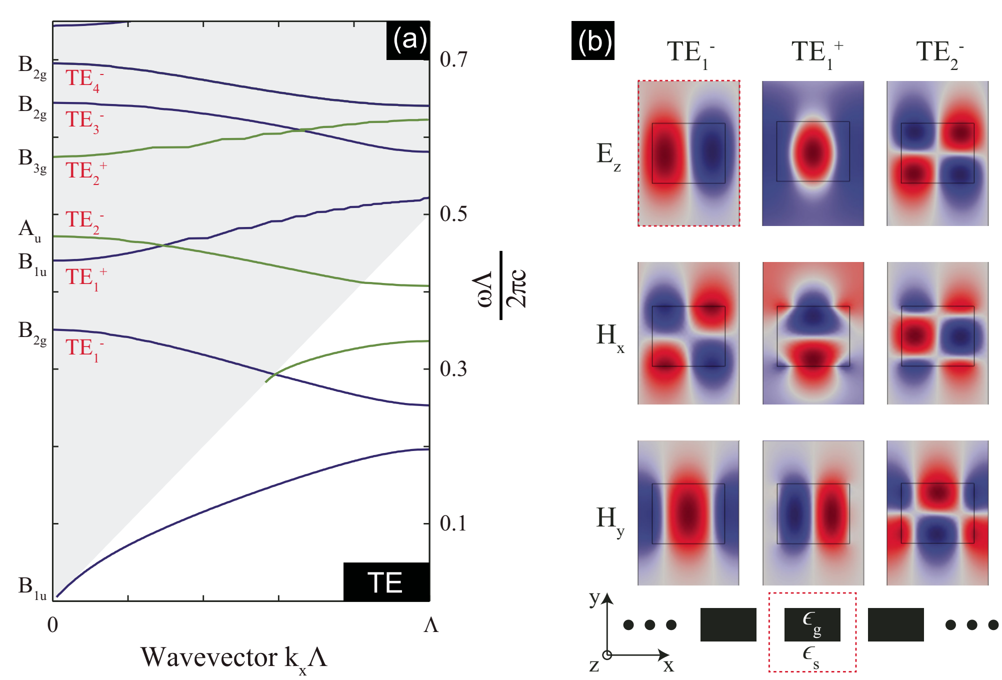

FIG. 3. (Color online) TE dispersion relations and select field profiles for a grating with $\frac{t}{\Lambda} = 0.6$, $FF = 0.72$, $\epsilon_g = 11.7$, and $\epsilon_s = 1$. (a) The dispersion relations include even (blue) and odd (green) bands with respect to reflection across $y = 0$. The modes at $k_x = 0$ are labeled with their Γ point (D_{2h} symmetry) irreducible representations and band definitions. The light cone is shown in light gray. (b) TE mode field profiles at $k_x = 0$ with a black line indicating the boundary between high and low permittivity regions. Below: grating simulation element, and directions defined.

TABLE IV. (a) C_s^{yz} character table and the analyzed grating modes associated with each irreducible representation, and (b) the compatibility relations between Point III and the Γ point.

C_s^{yz}	E	σ_x	TM Modes	TE Modes	Point III	Γ
A'	1	1	TM_2^-, TM_1^-	TE_1^+, TE_2^+	A'	$A_g, B_{3g}, \; B_{1u}, B_{2u}$
A''	1	−1	TM_1^+, TM_2^+, TM_3^-	TE_1^-, TE_2^-, TE_3^- TE_4^-	A''	$A_u, B_{1g}, \; B_{2g}, B_{3u}$
			(a)		(b)	

is allowed while modes TE_1^+ and TE_2^+ remain symmetry protected due to their antisymmetry in H_y across the yz plane. To couple to these additional modes, the x symmetry must also be broken, which could be achieved by introducing an additional k_x component to the wave vector. A summary of the permissible mode coupling for incident plane waves with wave vectors at Points I, II, and III is given in Table V.

III. TRANSMISSION FILTERING

We have leveraged this selective mode coupling to realize transmission filters using a dielectric grating. The operating principle, which has also been used in previously proposed dielectric transmission filter designs, involves coupling the incident light to two grating modes that overlap in frequency and have different coupling strengths. The strongly coupled mode produces a broad reflectance resonance, and Fano interference with the weakly coupled mode produces a narrow transmission peak within this high reflectance background. Previous proposals achieved the overlapping strong and weak resonances by coupling modes of different diffractive orders [20], using asymmetric grating structures [26], or combining a grating with additional resonant structures [19,27,28]. In contrast to these methods, we exploit symmetry-protected modes of a single diffraction order to achieve the required coupling strength disparity.

Figure 4 shows the transmittance profiles in the k_x and k_z directions, or moving towards Points II and III, respectively, for the transmission filter design discussed below. The imaginary part of the propagation constant, determined from the modal analysis, represents the coupling strength to the radiation field; a large (small) value results in fast (slow) decay and consequently a broadband (narrow-band) response. The width of a given resonance can be expressed by its quality factor, $Q = \frac{\omega}{\Delta\omega}$, and is related to the energy decay within the mode given by $U(t) = U(t_0)\exp[-\frac{\omega(t-t_0)}{Q}]$ [4]. We iteratively optimized the grating dimensions to maximize the coupling strength to accessible TM modes at normal incidence, Point I, and consequently achieve a very low-Q response. The structure exhibits broadband reflectance greater than 95% for $0.357 < \frac{\omega\Lambda}{2\pi c} < 0.625$. The optimized structure dimensions are identical to those used for the dispersion relations of Figs. 2 and 3: $\frac{t}{\Lambda} = 0.6$ and $FF = 0.72$. To facilitate the experimental demonstration discussed in the next section, we also included a substrate separated from the grating by an air layer of thickness $\frac{h}{\Lambda} = 0.8$, which is far enough to inhibit energy leakage from the grating. A permittivity of $\epsilon_g = 11.7$ was used for the grating and substrate, consistent with silicon in the infrared regime [29]. At normal incidence the low-transmittance background is demonstrated as a result of the optimized coupling to the TM_1^+ and TM_2^+ modes. From the group theoretical analysis we also expect coupling to mode TM_3^-. The transmission band associated with this mode exhibits a narrow-band response that is a result of a small overlap integral between the incident plane wave and mode. This small overlap integral can be inferred from the multiple nodes in the field profiles compared to an incident plane wave with wavelength greater than the grating thickness.

Away from normal incidence, $|k_x| > 0$ or $|k_z| > 0$, the relaxed selection rules enable coupling to the symmetry-protected modes. The broadband low transmittance is maintained near $k_x = k_z = 0$ since the overlap integrals with the modes responsible for the response remain nearly constant, $\cos(\theta) \approx 1$. Within this broadband background, narrow transmission bands emerge as a result of weak coupling to the symmetry-protected modes. These transmission bands are labeled with the modes responsible for the resonant response. A perturbation to normal incidence will leave the mode profiles nearly identical to the zone center ($k_x = k_z = 0$) modes, ensuring the overlap integral remains small and the associated coupling is weak. Thus, resonant high-Q transmission peaks are observed near normal incidence, and the peaks widen as $|k_x|$ or $|k_z|$ increases. Interestingly, the overlap integrals for the two sets of modes, TM and TE, result from different

TABLE V. Summary of the allowable mode coupling for a TM polarized plane wave with various incident wave vectors. X indicates relatively strong coupling, while x indicates relatively weak coupling. (Note that coupling to mode TM_3^- is allowed by symmetry even at normal incidence, but is relatively weak as described in the text.)

Modes	TM_1^-	TM_1^+	TM_2^-	TM_2^+	TM_3^-	TE_1^-	TE_1^+	TE_2^-	TE_2^+	TE_3^-	TE_4^-
Point I		X		X	x						
Point II	x	X	x	X	x						
Point III		X		X	x	x		x		x	x

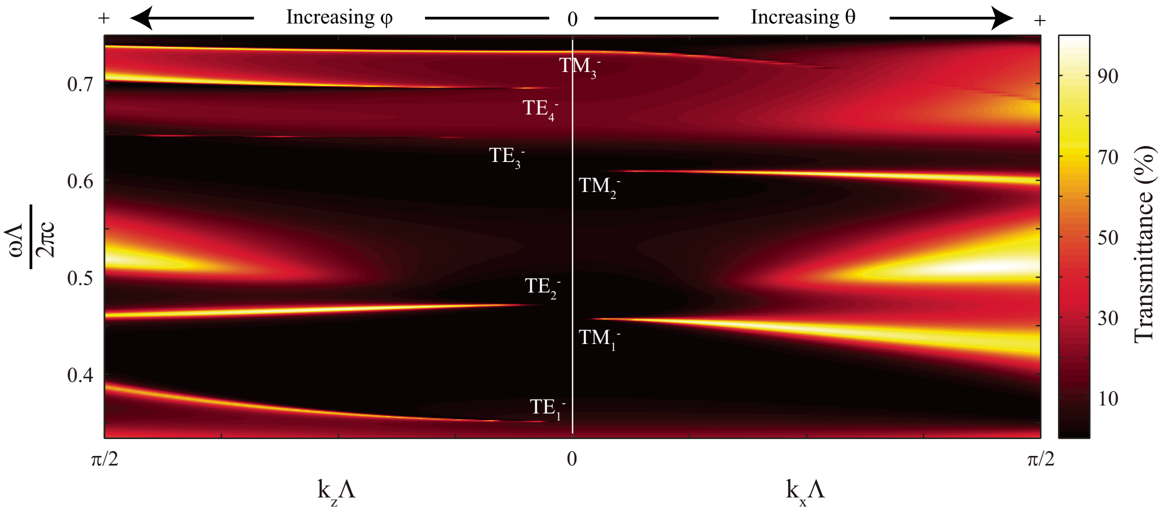

FIG. 4. (Color online) Simulated grating transmittance profile at normal and off-normal incidence. $k_x = k_z = 0$, $|k_x| > 0$, and $|k_z| > 0$ correlates to Points I, II, and III, respectively. The top scale shows increasing θ and φ directions corresponding to $|k_x| > 0$, and $|k_z| > 0$, respectively. Transmission bands are labeled with the mode associated with the resonance.

mechanisms. For the TM cases, the off-normal incidence simply results in nonzero overlap integrals for every field component while the TE cases result from a small polarization overlap between the incident field and modes due to magnetic field depolarization when k_z is introduced.

The agreement between the simulated transmittance and the modal analyses is strong. The transmittance bands for $|k_x| > 0$ align exceptionally well with the dispersion relations of Fig. 2, with deviations only observed for the estimated TM_1^+ and TM_2^+ bands. The transmittance bands associated with the TE modes are also in excellent agreement with the zone center ($\boldsymbol{k} = 0$) frequencies of the TE dispersion relations. Furthermore, the TM_3^- coupling responsible for the transmittance band at $\frac{\omega\Lambda}{2\pi c} = 0.72$ persists as $|k_z|$ is increased, explicitly showing how the TM mode coupling is maintained while TE mode coupling is introduced. Notably, one would expect the transmission bands for $|k_z| > 0$ to increase in frequency with increasing $|k_z|$ due to the lack of periodicity in the z direction. However, both TE_2^- and TE_4^- transmission bands initially decrease in frequency away from normal incidence. We attribute this decrease to avoided crossings between these modes and the TM_1^+ and TM_3^- modes, which have the same symmetry within the C_s^{yz} point group and are slightly higher in frequency.

IV. EXPERIMENTAL DEMONSTRATION

We based the experimental demonstration on a suspended silicon grating fabricated from a silicon-on insulator platform that operates in the long-wavelength infrared spectrum (LWIR, 8–14 μm). This spectral range has technological importance in thermal imaging, surveillance and remote sensing [30,31]. The grating geometry was defined using standard photolithography and reactive ion etching, while subsequent hydrofluoric acid etching suspended the 250×500 μm silicon grating slab. Scanning electron microscopy was used to optimize the structure fabrication. To characterize the structure's electromagnetic response we used a commercial Fourier transform infrared (FTIR) spectrometer with a microscope attachment and a wire grid polarizer. The spectrometer resolution was 4 cm^{-1}. Additionally, a custom-made sample holder and an iris placed above the sample were used to constrain the light from the microscope's high numerical aperture ($NA = 0.6$) Cassegrain objectives. The effective numerical aperture including the extra iris was approximately $NA = 0.05$, corresponding to a spread in the incident angle of $\pm 3^\circ$. The iris location was manipulated using an xyz-translation stage with micrometer adjustment, which enabled independent control of k_x and k_z using the incident angles θ and φ defined in Fig. 1(a).

Figure 5 shows the experimental and simulated transmittance for a grating with dimensions $\Lambda = 4.9$ μm, $t = 2.85$ μm, $h = 4.05$ μm, and $FF = 0.72$ and incident light configurations analyzed: Points I, II, and III, as well as a fourth point, Point IV ($\theta, \varphi > 0^\circ$). The inset shows a scanning electron micrograph of a representative suspended grating. In contrast to the preceding analyses that defined the incident field using the wave vector, the experimental demonstration had the incident field defined by θ and φ. As a consequence, the plot labels of Fig. 5 do not represent a single point in k space, but instead they represent a range of incident wave vectors confined to the $k_x k_y$ and $k_y k_z$ planes for Points II and III, respectively.

In the absence of nonradiative losses, the quality factors of the peaks associated with the symmetry protected modes are expected to increase infinitely as the incident light approaches normal incidence [4]. However, when the radiative coupling becomes less than the nonradiative losses, the peak height begins to decrease without appreciable further reductions in the peak width. The incidence angles reported in Fig. 5 are those for which the nonradiative and radiative losses are of the same order of magnitude, as discussed further below.

At normal incidence, Point I ($\theta = \varphi = 0^\circ$), the low-transmittance background is demonstrated to be below 7% between 8 and 13 μm, which agrees well with the simulated transmittance. The corresponding simulated response has been

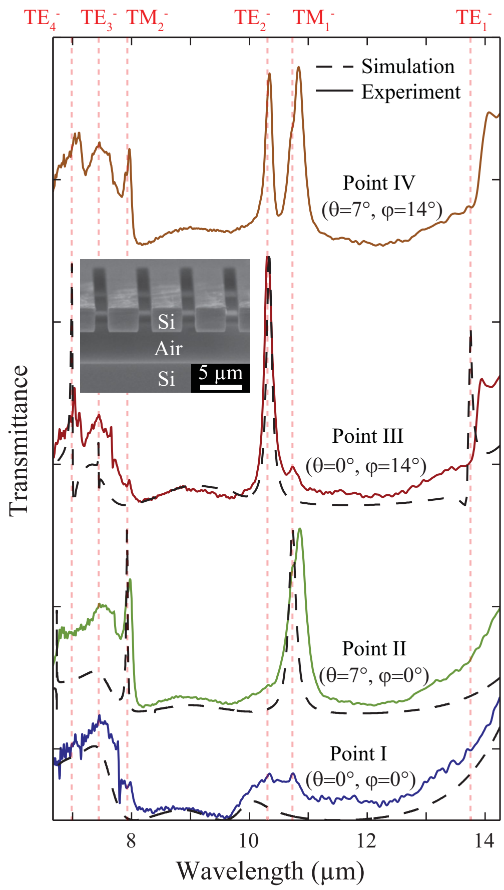

FIG. 5. (Color online) Experimental and associated simulated transmittance of a grating with various incident wave configurations. The as-built dimensions were $\Lambda = 4.9\ \mu$m, $t = 2.85\ \mu$m, $h = 4.05\ \mu$m and $FF = 0.72$. Broadband reflectance, TM selective filtering, TE selective filtering and mixed TE and TM filtering are demonstrated, which are associated with the various points in the Brillouin zone: Point I ($\theta = \varphi = 0^\circ$, Point II ($\theta = 7^\circ, \varphi = 0^\circ$), Point III ($\theta = 0^\circ, \varphi = 14^\circ$), and Point IV ($\theta = 7^\circ, \varphi = 14^\circ$), respectively. Inset: scanning electron micrograph of a representative suspended grating.

reduced to 70% of its calculated value to account for the reflection loss at the substrate's exit interface, which was not included in the simulation due to computational demands. The experimental response at Point II ($\theta = 7^\circ, \varphi = 0^\circ$) is similarly shown to agree with its as-built simulation. In this case the transmittance has been normalized to the peak transmittance of the experimental results (26%) to accentuate the qualitative agreement between the data sets. The experimental response exhibits the transmission bands associated with both the TM_1^- and TM_2^- with moderate broadening and wavelength shifts compared to the simulation that will be explained below. Similarly moving to Point III ($\theta = 0^\circ, \varphi = 14^\circ$) demonstrates selective coupling to TE modes as we expect. Modes TE_1^- and TE_2^- are clearly demonstrated and signatures of modes TE_3^- and TE_4^- are observable with the normalized simulated response (36.5%) agreeing well with the data. For both TM and TE demonstrations, the transmission band frequencies are within 1% of those determined from the modal analysisi, which is within the experimental error of measuring the gratings dimensions. To ensure the resonant response results from two separate mode sets, we took data at Point IV ($\theta = 7^\circ, \varphi = 14^\circ$), which introduces k_x and k_z simultaneously. The corresponding data exhibit transmission bands associated with both TM and TE mode sets, confirming the independence of the mode coupling at Points II and III. At the further reduced symmetry of Point IV we would also expect resonant transmission bands from modes TE_1^+ and TE_2^+ as mentioned in the group theoretical analysis of TE mode coupling. Unfortunately, due to the small overlap integrals in both the k_x and k_y directions, the resulting quality factors were too high to be resolved experimentally.

There is strong agreement between the experimental and simulated structure response, however, several of the expected peaks are not well defined and the experimental quality factors are lower than those simulated. The maximum demonstrated quality factors for the two dominant transmission bands centered in the opaque background, associated with coupling to TM_1^- and TE_2^- modes, were $Q_{exp}(\theta = 7^\circ) = 33$, and $Q_{\text{exp}}(\varphi = 14^\circ) = 64$, respectively. These are smaller than their expected quality factors due to resonance broadening, $Q_r(\theta = 7^\circ) = 113$, and $Q_r(\varphi = 14^\circ) = 107$. The reduction in the quality factor can be attributed to the angular extent allowed by the aperture, nonradiative losses that can dominate the response at lower angles, and the finite grating size.

The $\pm 3^\circ$ angular uncertainty allowed by the iris setup, discussed above, is expected to significantly affect the resonant response. A range of angles probes different k_x or k_z values, which due to the slope of the transmission bands of Fig. 4 is expected to result in a broader observed peak. This angular dependence is evident in the experimental data, where the transmission peak corresponding to the TE_2^- mode is narrower and more symmetrical than the peak corresponding to the TM_1^- mode. The highest possible measured quality factors allowed by the iris's angular extent are $Q_i(\theta = 7 \pm 3^\circ) \approx 110$, and $Q_i(\varphi = 14 \pm 3^\circ) \approx 175$, for TM and TE modes respectively.

Even with better angular control of the incident light, material absorption and inhomogeous broadening due to disorder scattering are still expected to put an upper bound on the achievable quality factor as $\theta,\varphi \to 0^\circ$. Using optical properties from the literature for silicon in this frequency range [29], the maximum quality factor due to nonradiative losses is on the order $Q_{nr} \sim 10^4$. This estimate serves as an upper bound, and does not include additional absorption losses due to dopants or impurities introduced during the fabrication process, nor does it include scattering losses due to manufacturing imperfections. Using the relation $1/Q_{\text{tot}} = 1/Q_r + 1/Q_{nr}$, we estimate the nonradiative quality factor in our samples to be $Q_{nr} \sim 100$. Optimizing the fabrication further to reduce surface roughness and improve sidewall profiles may increase the transmittance and quality factor.

It is also known that the grating size affects the attainable quality factor and peak transmittance on resonance [32,33]. Since our grating was limited to approximately 100 periods, this could further limit our peak transmittance and quality factor.

However, despite the experimental limitations that make resolving the higher quality factor resonances more challenging, we were able to observe expected signatures from all but the two highest-Q resonances.

V. CONCLUSION

We have demonstrated selective coupling to symmetry-protected modes of a dielectric grating to realize transmission filtering capabilities. Using a group theoretical analysis, we determined the selection rules that govern plane wave coupling to the grating's supported modes. Using these selection rules, we maximized the coupling strength to modes accessible at normal incidence to provide a low-transmittance background. Introducing a perturbation to normal incidence in the k_x ($\theta > 0^\circ$) or k_z ($\varphi > 0^\circ$) directions, weak coupling to TM and TE symmetry protected modes, respectively, was shown to result in high-Q transmission peaks within the low-transmittance background. We simulated and experimentally verified the grating's transmission filtering capabilities at various incidence angles, which were shown to agree well with each other and the modal analysis. Although we have chosen to relax the symmetry by introducing off-normal incident light, similar response is expected at normal incidence if instead the grating's symmetry is broken. This could be achieved by changing the period and fill factor across the extent of the grating or by etching the grating at an angle to break the symmetry across the yz plane, σ_x.

Furthermore, we note that other types of infinite-Q modes have been observed above the light line in photonic crystal slabs, that are not due to symmetry protection and occur away from normal incidence [34]. It may be possible to exploit such modes to create similar filters at arbitrary incidence angles.

These transmission filters have potential to be used in a wide array of applications. While our demonstration was performed in the LWIR, the operating principle is scalable to any wavelength range, if similarly lossless materials are available. In the LWIR, these filters may enable improved hyperspectral imaging capabilities for remote sensing and surveillance applications [30,31]. Hyperspectral imaging records the electromagnetic spectrum for every point in a viewing plane, providing enhanced discrimination between objects. These single-layer filters have potential to be integrated at the pixel or subpixel level, which may lead to improved and more cost-effective imaging capabilities. Additionally, selective emitters/absorbers are expected to increase the efficiency of thermophotovoltaics [35–38]. These gratings may enhance selective emitting/absorbing capabilities for these applications over similar two-dimensional structures by exploiting the higher density of states afforded by one-dimensional structures.

ACKNOWLEDGMENTS

J.M.F. acknowledges a Rackham Merit Fellowship. S.M.Y. acknowledges support from the MRSEC Program of the National Science Foundation under Grant No. DMR-1120923. Grating fabrication and characterization were supported as part of the Center for Solar and Thermal Energy Conversion, an Energy Frontier Research Center funded by the U.S. Department of Energy, Office of Science under Award No. DE-SC0000957. All device fabrication was carried out in the Lurie Nanofabrication Facility at the University of Michigan.

[1] J. D. Joannopoulos, S. G. Johnson, J. N. Winn, and R. D. Meade, *Photonic Crystals: Molding the Flow of Light*, 2nd ed. (Princeton University Press, Princeton, 2008).
[2] E. Yablonovitch, Phys. Rev. Lett. **58**, 2059 (1987).
[3] S. John, Phys. Rev. Lett. **58**, 2486 (1987).
[4] K. Sakoda, *Optical Properties of Photonic Crystals*, Springer Series in Optical Sciences (Springer, Bellingham, Washington, 2005).
[5] U. Fano, Phys. Rev. **124**, 1866 (1961).
[6] S. Fan and J. D. Joannopoulos, Phys. Rev. B **65**, 235112 (2002).
[7] S. Fan, W. Suh, and J. D. Joannopoulos, J. Opt. Soc. Am. A **20**, 569 (2003).
[8] R. Magnusson and S. S. Wang, Appl. Phys. Lett. **61**, 1022 (1992).
[9] T. Ochiai and K. Sakoda, Phys. Rev. B **63**, 125107 (2001).
[10] P. Paddon and J. F. Young, Phys. Rev. B **61**, 2090 (2000).
[11] J. Lee, B. Zhen, S. L. Chua, W. Qiu, J. D. Joannopoulos, M. Soljačić, and O. Shapira, Phys. Rev. Lett. **109**, 067401 (2012).
[12] J. M. Foley, S. M. Young, and J. D. Phillips, Appl. Phys. Lett. **103**, 071107 (2013).
[13] B. Zhen, S.-L. Chua, J. Lee, A. W. Rodriguez, X. Liang, S. G. Johnson, J. D. Joannopoulos, M. Soljačić, and O. Shapira, Proc. Nat. Acad. Sci. USA **110**, 13711 (2013).
[14] C. F. R. Mateus, M. C. Y. Huang, L. Chen, C. J. Chang-Hasnain, and Y. Suzuki, IEE Photonics Technology Letters **16**, 1676 (2004).
[15] M. C. Y. Huang, Y. Zhou, and C. J. Chang-Hasnain, Nature Photon. **1**, 119 (2007).
[16] D. Fattal, J. J. Li, Z. Peng, M. Fiorentino, and R. G. Beausoleil, Nature Photon. **4**, 466 (2010).
[17] F. L. Lu, F. G. Sedgwick, V. Karagodsky, C. Chase, and C. J. Chang-Hasnain, Opt. Express **18**, 12606 (2010).
[18] M. Shyiq Amin, J. Woong Yoon, and R. Magnusson, Appl. Phys. Lett. **103**, 131106 (2013).
[19] S. Tibuleac and R. Magnusson, Opt. Lett. **26**, 584 (2001).
[20] Y. Ding and R. Magnusson, Opt. Lett. **29**, 1135 (2004).
[21] J. S. Ye, N. Matsuyama, Y. Kanamori, and K. Hane, IEEE Photonics Technol. Lett. **20**, 851 (2008).
[22] Y. Kanamori, T. Kitani, and K. Hane, Jpn. J. Appl. Phys. **45**, 1883 (2006).
[23] Y. Kanamori, M. Shimono, and K. Hane, IEEE Photonics Technol. Lett. **18**, 2126 (2006).
[24] M. Davanco, Y. Urzhumov, and G. Shvets, Opt. Express **15**, 9681 (2007).
[25] G. Parisi, P. Zilio, and F. Romanato, Opt. Express **20**, 16690 (2012).
[26] Y. Ding and R. Magnusson, Opt. Express **12**, 1885 (2004).
[27] S. Boutami, B. Benbakir, X. Letartre, J. L. Leclercq, P. Regreny, and P. Viktorovitch, Opt. Express **15**, 12443 (2007).

[28] L. Pilozzi, D. Schiumarini, N. Tomassini, and A. D'Andrea, Phys. Rev. B **86**, 045301 (2012).

[29] E. D. Palik, *Handbook of Optical Constants of Solids* (Academic Press, 1998).

[30] M. Vollmer and K. Mllmann, *Infrared Thermal Imaging: Fundamentals, Research and Applications* (Wiley, Weinheim, 2011).

[31] M. T. Eismann, *Hyperspectral Remote Sensing* (SPIE Press, Bellingham, Washington, 2012).

[32] D. K. Jacob, S. C. Dunn, and M. G. Moharam, J. Opt. Soc. Am. A **17**, 1241 (2000).

[33] J. O. Grepstad, M. M. Greve, B. Holst, I. R. Johansen, O. Solgaard, and A. Sudbo, Opt. Express **21**, 23640 (2013).

[34] C. W. Hsu, B. Zhen, J. Lee, S. L. Chua, S. G. Johnson, J. D. Joannopoulos, and M. Soljačić, Nature (London) **499**, 188 (2013).

[35] N.-P. Harder and P. Würfel, Semicond. Sci. Technol. **18**, S151 (2003).

[36] Y. X. Yeng, W. R. Chan, V. Rinnerbauer, J. D. Joannopoulos, M. Soljačić, and I. Celanovic, Opt. Express **21**, A1035 (2013).

[37] V. Rinnerbauer, S. Ndao, Y. X. Yeng, W. R. Chan, J. J. Senkevich, J. D. Joannopoulos, M. Soljacic, and I. Celanovic, Energy Environ. Sci. **5**, 8815 (2012).

[38] V. Rinnerbauer, Y. X. Yeng, W. R. Chan, J. J. Senkevich, J. D. Joannopoulos, M. Soljačić, and I. Celanovic, Opt. Express **21**, 11482 (2013).